THE PENNSYLVANIA STATE UNIVERSITY
SCHREYER HONORS COLLEGE

DEPARTMENT OF MECHANICAL AND NUCLEAR ENGINEERING

COMPUTATIONAL ANALYSIS OF POWER ATTENUATION DURING DIRECTED ENERGY DEPOSITION

Christopher Kozuch
Spring 2016

A thesis
submitted in partial fulfillment
of the requirements
for a baccalaureate degree
in Mechanical Engineering
with honors in Mechanical Engineering

Reviewed and approved* by the following:

Timothy W. Simpson
Professor of Mechanical and Nuclear Engineering
Professor of Industrial and Manufacturing Engineering
Thesis Supervisor

Zoubeida Ounaies
Professor of Mechanical Engineering
Honors Adviser

*Signatures are on file in the Schreyer Honors College.

Abstract

Directed energy deposition (DED) is a type of metal additive manufacturing that uses a laser to continuously fuse a stream of metal powder to a workpiece, thereby building a component layer by layer. The attenuation coefficient is a process parameter that describes the reduction of the laser power as it passes through the powder. This work presents a method for calculating the attenuation coefficient by discretizing the laser into numerous rays and tracing the rays through the powder. The method was applied to iron and copper powders with normally distributed sizes that were irradiated by CO_2 and Nd:YAG lasers. The results were compared against experimental values, and the average absolute error was found to be 24.2%. Although this error is higher than optimal, it is low enough to develop trends. One such trend was developed for the dependence of the attenuation coefficient on the refractive index of the metal powder. The development of a trend such as this demonstrates that computational ray tracing can be used to assist in the analysis of the DED process.

Table of Contents

List of Figures

List of Tables

Acknowledgements

I would like to express my sincere gratitude to my research adviser, Dr. Richard Martukanitz, my thesis adviser, Dr. Timothy W. Simpson, and my honors adviser, Dr. Zoubeida Ounaies. I would also like to acknowledge the invaluable assistance and funding provided by the collaboration of the Penn State Applied Research Laboratory and the Center for Innovative Materials Processing Through Direct Digital Deposition (CIMP-3D).

Chapter 1

Introduction

1.1 Background

The term additive manufacturing is usually used to refer to a method of constructing components layer-by-layer from a feedstock material [1]. There currently exist many techniques for many materials, but the techniques for metal additive manufacturing have been classified by ASTM Committee F42 as either powder bed fusion or directed energy deposition (DED) [2]. The methods presented in this work have been developed for DED.

The DED process uses a focused laser to fuse successive layers of metal feedstock to a substrate. For each layer, the feedstock is continuously fed underneath the laser as it proceeds along a preprogrammed path [3]. The feedstock can take the form of wire or powder, but this work is focused solely on the powder case.

1.2 Motivation

The additive manufacturing market is growing at an astounding rate. The 2015 Wohlers Report estimated that the industry grew by 32.5% in 2014 [4]. Astoundingly, the metal additive manufacturing market is growing even faster, with a growth of nearly 89% in 2014, according to SmarTech Markets Publishing [5]. This has spurred an intense interest in research and development, but experimentation costs are currently very high. Therefore, the focus has shifted towards computational simulation. Recent research has concentrated on finite element and finite volume methods [6] [7] [8] [9]. These methods require a model for the heat source produced by the laser. The heat source models normally depend on a number of parameters, including an attenuation coefficient, γ, which describes how quickly the laser power decreases with depth.

The attenuation coefficient can be determined experimentally, but it is often more cost effective to obtain it via computational simulation. Early work by Zhou et al. in 2009 showed that this could be achieved for monodispersed powders by discretizing the laser into rays and tracing the rays through the powder [10]. This work was recently extended to include polydispered powders by Moser et al. [11]. However, both of these analyses assumed that the power absorbed by a given particle was independent from the impacting ray's angle of incidence. Zhodi demonstrated in 2013 that Fresnel's Equations could be used to account for the angle of incidence [12], but his analysis, like that of Zhou et al., assumed that all of the particles were of equal size, which is often not the case. Therefore, this work seeks to implement a model that both employs a realistic powder distribution and accounts for angle of incidence when performing absorption calculations.

1.3 Test Cases

In 2007, McVey et al. carried out several experiments that employed DED with preplaced powder [13]. Various distributions of copper and iron powder were irradiated with a CO_2 ($10.6\,\mu m$) or Nd:YAG ($1.06\,\mu m$) laser. For each case, the intensity was measured at regular depth intervals, and the attenuation coefficient was calculated from the results (see Section 2.2 for more details). The reported values are given in Table 1.1. These values serve as a basis for validation of the computational method presented in this work. Table 1.2 shows the ranges in which the data was collected.

Table 1.1: Values for Curve Fits of Experimental Data [13]

Powder	Laser	γ (m^{-1})	R^2
Copper	CO_2	1.30E+04	0.836
	Nd:YAG	1.13E+04	0.856
Iron	CO_2	1.44E+04	0.921
	Nd:YAG	1.73E+04	-3.844

Table 1.2: Experimental Depth Limits [13]

Powder	Laser	Minimum (μm)	Maximum (μm)
Copper	CO_2	100	450
	Nd:YAG	150	500
Iron	CO_2	150	450
	Nd:YAG	200	500

1.4 Overview

The remainder of this thesis has been split into four chapters. Chapter 2 describes the optical theory that was used for this work, and it presents the system that was used to quantify attenuation. Chapter 3 provides the methodology that was used to produce the powder packings, discretize the the laser into rays, and trace the rays through the powder. Chapter 4 gives the results generated through the application of the process described in Chapter 3 and develops trends for the relationship between attenuation and refractive index. Finally, Chapter 5 discusses the implications of the results and outlines possible future work.

Chapter 2

Theoretical Development

This chapter covers two topics. First, it presents the optical theory required to calculate the interaction between electromagnetic rays and particles, which includes the Law of Reflection, Snell's Law, and Fresnel's Equations. Second, it details the format that was used to measure the attenuation of the beam as it passes through the powder.

2.1 Ray-Particle Interaction

The principle assumption for ray-tracing analysis is that the electromagnetic beam produced by the laser during DED can be decomposed into discrete rays. (Proof of convergence for this method is given in Section 4.1.) The challenge is therefore to simulate the trajectory and power level of the ray as it passes through the powder. The chamber is filled with inert gas during the build process, but the gas's optical properties are so similar to a vacuum that it will be approximated as such. As a result, the rays do not change course or lose power as they pass through the space between particles. Therefore, the only way a ray's trajectory or power level can be changed is through a collision with a particle (collisions between rays are not considered).

Figure 2.1 shows the result of a ray-particle collision. The incident ray, R_i, and the incident angle, θ_i, are known, but the remaining elements have to determined. This can be achieved through the application of three equations. The first, and simplest, is the Law of Reflection, which is shown in Equation 2.1. It allows the reflected angle, θ_r, to be resolved.

$$\theta_i = \theta_r \tag{2.1}$$

The second equation, Equation 2.2, is Snell's Law [14]. In this case, n_i is the index of refraction for the environment and n_t is the index of refraction for the particle. Using these parameters, along with the incident angle, Snell's Law enables us to solve for the angle of refraction, θ_t.

$$\frac{\sin\theta_i}{\sin\theta_t} = \frac{n_t}{n_i} \tag{2.2}$$

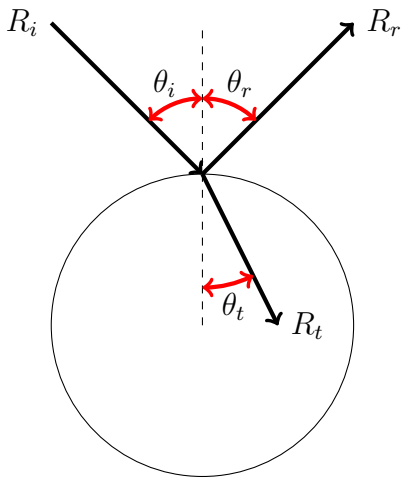

Figure 2.1: Refraction Diagram

The combination of the Law of Reflection and Snell's Law allows the geometry of the system to be completely resolved, but the power carried by the produced rays is still unknown. For that, the last equation, really a set of equations, is required. The Fresnel Equations, given in Equation 2.3 and Equation 2.4, describe the fraction of power reflected for s polarized light, R_s, and p polarized light, R_p [15]. The bar accent denotes the complex conjugate. Equation 2.3 and Equation 2.4 have been simplified using the assumption that the magnetic permeability of the material is approximately equal to that of the surrounding environment, which is fairly accurate for the materials under consideration in this study.

$$R_s = r_s\overline{r_s} \qquad r_s = \left|\frac{n_i\cos\theta_i - n_t\cos\theta_t}{n_i\cos\theta_i + n_t\cos\theta_t}\right| \tag{2.3}$$

$$R_p = r_p\overline{r_p} \qquad r_p = \left|\frac{n_i\cos\theta_t - n_t\cos\theta_i}{n_i\cos\theta_t + n_t\cos\theta_i}\right| \tag{2.4}$$

However, the irradiation from the laser can be considered unpolarized with respect to its axis; so, the fraction of power reflected is equal to the average of that for s polarized and p polarized light. This relationship is given in Equation 2.5. Since energy must be conserved, the fraction of power diverted to the transmitted ray is given by Equation 2.6.

$$R = \frac{R_s + R_p}{2} \tag{2.5}$$

$$T = 1 - R \tag{2.6}$$

For the purposes of this analysis, we assume that the transmitted ray is completely absorbed by the particle. This assumption comes from an analysis of the absorption coefficient, α, for each of the materials in question, copper and iron. Table 2.1 gives the values for this and the indices of refraction for both copper and iron. Equation 2.7 gives the transmitted intensity, $I(z)$, as a function of the depth, z, incident intensity, I_0, and the absorption coefficient [16].

$$I(z) = I_0\exp\left(-\alpha z\right) \tag{2.7}$$

Rearranging Equation 2.7 allows us to obtain an expression for depth as a function of fractional attenuation, as shown in Equation 2.8.

$$z = \frac{\ln\left[I(z)/I_0\right]}{-\alpha} \tag{2.8}$$

Since iron under a $10.6\,\mu\mathrm{m}$ beam has the smallest absorption coefficient in Table 2.1 with a value of 34.957 $\mu\mathrm{m}^{-1}$, the maximum depth that just 1% of the initial intensity can be transmitted is 0.13 $\mu\mathrm{m}$. However, 95% of the iron particles are larger than 12 $\mu\mathrm{m}$, which is nearly two orders of magnitude larger; so, it is safe to assume that none of the refracted rays pass through any of the particles.

Additionally, since we approximated the environment as a vacuum, $n_i = 1$ in Equations 2.2 to 2.4. Figure 2.2 plots the fraction of power reflected and absorbed against the the index of refraction of the particles for an incident angle of $\theta_i = 0$. However, the incident angle is obviously not always zero. Figure 2.3 shows the reflected power plotted against the incident angle for a

Table 2.1: Refractive Indices and Attenuation Coefficients for Solid Copper and Iron [17]

λ (µm)	Cu		Fe	
	n	α (µm^{-1})	n	α (µm^{-1})
1.06	0.3755	83.419	3.2315	51.111
10.6	9.4305	80.330	7.3703	34.957

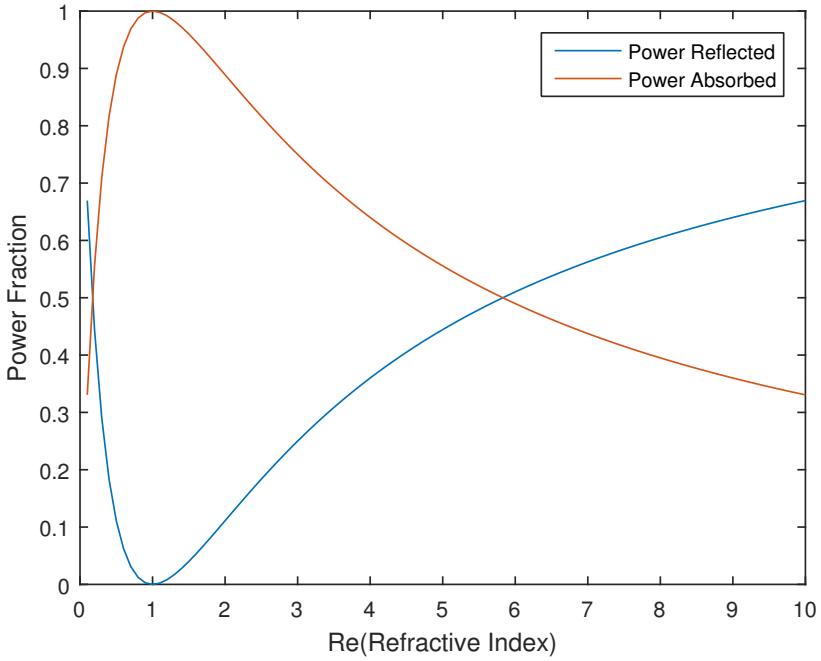

Figure 2.2: Reflected and Absorbed Power vs. Particulate Index of Refraction for $\theta_i = 0$

number of indices. Notice that the curves for large indices of refraction each show a local minimum. The angles at which these minimums occur are equal to Brewster's Angle, which is given Equation 2.9, because that is the angle at which p polarized light is completely absorbed [18]. This phenomenon is much more difficult to observe for smaller indices of refraction because p polarized light constitutes a smaller fraction of reflected light in that case.

$$\theta_B = \arctan\left(\frac{n_t}{n_i}\right) \tag{2.9}$$

2.2 Attenuation Quantification

Although the interaction between rays and particles can now be simulated, a system for quantifying the attenuation through the powder must be devised. To achieve this, we have implemented a modified version of Equation 2.7, which is shown in Equation 2.10. In this new form, the absorption coefficient, α, has been replaced by the attenuation coefficient, γ. Additionally, a correction

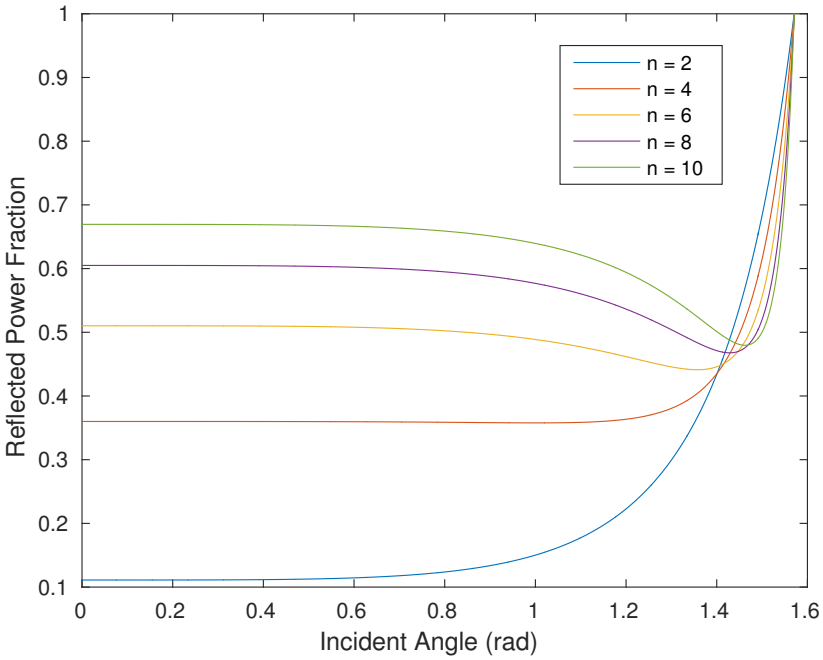

Figure 2.3: Reflected Power vs. Incident Angle for Various Indices of Refraction

term, β, has been inserted to capture data that does not fall on a perfect exponential curve.

$$I(z) = I_0 \beta \exp(-\gamma z) \tag{2.10}$$

Multiplying both sides of the relationship by the spot area converts it to a power basis, as shown in Equation 2.11. $P(z)$ is the power as a function of depth, and P_0 is the incident power.

$$P(z) = P_0 \beta \exp(-\gamma z) \tag{2.11}$$

The attenuation coefficient, γ, and the correction term, β, are obtained by curve-fitting experimental data. This is achieved by first converting Equation 2.11 to a linear form, as shown in Equation 2.12. The definitions of the parameters f, a_0, and a_1 are given in Equation 2.13.

$$f = a_0 + a_1 z \tag{2.12}$$

$$f = \ln \frac{P(z)}{P_0} \qquad a_0 = \ln \beta \qquad a_1 = -\gamma \tag{2.13}$$

Next, the coefficients a_0 and a_1 are obtained by applying the least squares regression method to Equation 2.11. Finally, the correction factor and attenuation coefficient are determined by evaluating Equation 2.14 and Equation 2.15, respectively.

$$\beta = \exp(a_0) \tag{2.14}$$

$$\gamma = -a_1 \tag{2.15}$$

2.3 Chapter Summary

In this chapter, the optical theories used to quantify the interactions between rays and particles were presented. These included the Law of Reflection, Snell's Law, and Fresnel's Equations. Additionally, the rationale for assuming that no rays pass through any particle was explained. Finally, the definition of the attenuation coefficient was given, and the system for obtaining it was described. The next chapter will present the methods used to create particle packings, discretize the laser into rays, and trace those rays through the powder.

Chapter 3

Methodology for Particle Packing, Beam Decomposition, and Ray Tracing

This chapter details the methods employed to perform the three most significant tasks of the simulation: particle packing generation, beam decomposition, and ray tracing. Additionally, the experimental parameters used to define the powder and laser are identified.

3.1 Particle Packing

The first step in constructing a simulation for the system under consideration is to create a particle packing that accurately represents the powder distribution. For the experimentation carried out by McVey et al. [13], two original distributions were used; one was composed of copper, and the other was composed of iron. Approximately 90% of the copper particles had a diameter between 10 and 150 µm, while 90% of the iron particles had a diameter between 12 and 240 µm. The distributions are assumed to be normal; so, the mean is given by the average of the bounds, as shown in Equation 3.1. Here, μ is the average diameter, d_{min} is the lower bound on the middle 90% of the distribution, and d_{max} is the upper bound of the middle 90% of the distribution.

$$\mu = \frac{d_{min} + d_{max}}{2} \tag{3.1}$$

Another result of this distribution data is that 5% of the diameters are less than d_{min}; so, the Z score associated with d_{min} is approximately -1.645. This can be used to calculate the standard deviation, σ, as shown in Equation 3.2.

$$\sigma = \frac{d_{min} - \mu}{Z} \tag{3.2}$$

The mean and standard deviation for both distributions were calculated using this method, and they are presented in Table 3.1. A graphical representation of this is shown in Figure 3.1.

Table 3.1: Particle Distribution Parameters

Powder	d_{min} (µm)	d_{max} (µm)	μ	σ
Copper	10	150	80	42.55
Iron	12	240	126	69.30

Once the distributions were known, the particles had to be packed to the proper density. This was accomplished through the implementation of Yade, an open source discrete element method code [19]. A bounding cylinder was constructed from facets, and a cloud of particles was generated within it in accordance with the distribution parameters. A flat plate, also constructed from facets, was then used to compress the cloud until it reached the proper porosity. McVey et al. reported a porosity of 0.46 for the copper packing and a porosity of 0.67 for the iron packing [13]; so, these were the target values that were used in this study. Before and after pictures for the copper and iron distributions are shown in Figure 3.2 and Figure 3.3, respectively.

3.2 Beam Decomposition

Since the laser system under consideration had an aperture placed after the beam splitter to ensure that the irradiated energy was evenly distributed [13], each ray was given the same incident

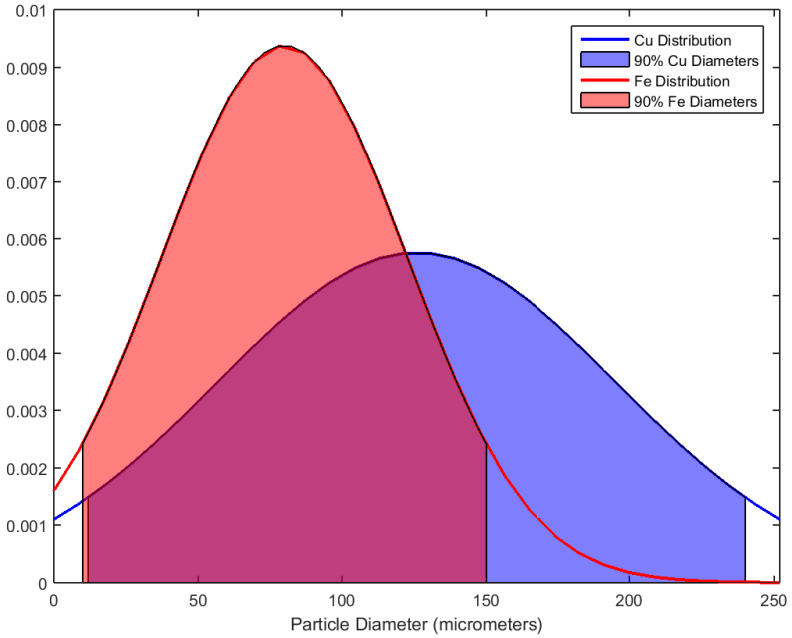

Figure 3.1: Particle Distributions

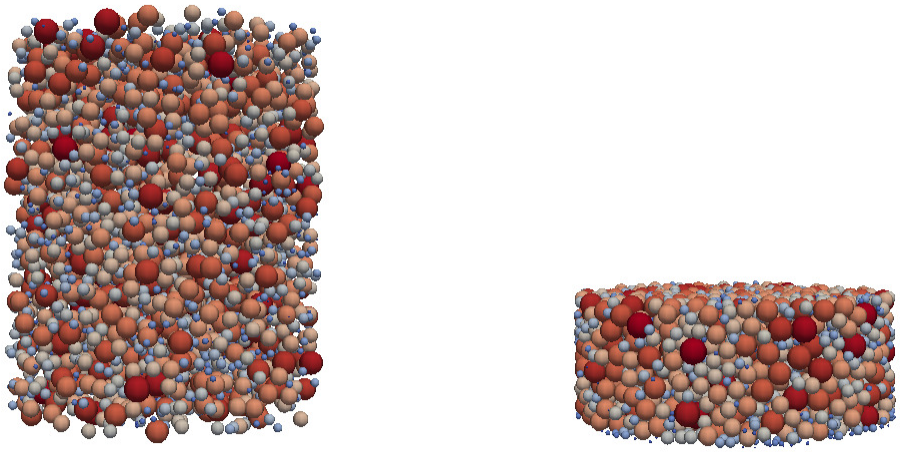

(a) Copper Particle Cloud

(b) Compacted Copper Particles

Figure 3.2: Compression of Copper Particle Cloud to Desired Density

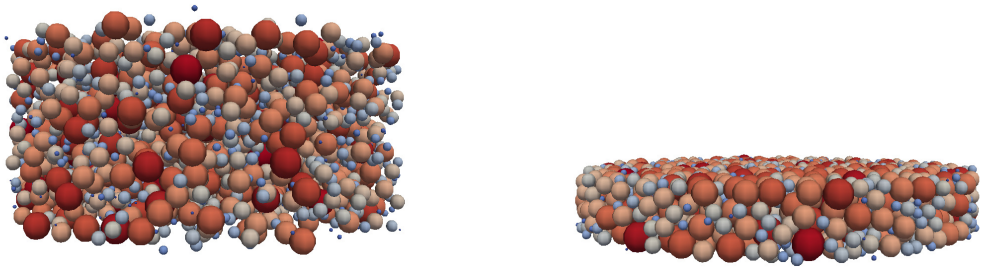

(a) Iron Particle Cloud

(b) Compacted Iron Particles

Figure 3.3: Compression of Iron Particle Cloud to Desired Density

power value. Additionally, the particle diameters were smaller than the spot diameter by more than an order of magnitude; so, the packing was effectively periodic within the spot area. To increase efficiency, a smaller simulation area was used, and the results were extended to the entire spot area (i.e., the actual area irradiated by the beam during experimentation). Therefore, the power carried by each ray is given by Equation 3.3, where P_{total} is the total power that impacts the spot area, N_{rays} is the number of rays, A_{sim} is the simulated area, and A_{real} is the spot area of the laser.

$$P_{ray} = \frac{P_{total}}{N_{rays}} \times \frac{A_{sim}}{A_{real}} \tag{3.3}$$

Since spot areas are usually described by their diameters, Equation 3.3 has been rewritten using D_{sim} for the simulated diameter and D_{real} for the spot diameter of the laser in Equation 3.4.

$$P_{ray} = \frac{P_{total}}{N_{rays}} \times \left(\frac{D_{sim}}{D_{real}}\right)^2 \tag{3.4}$$

In accordance with the experimentation conducted by McVey et al., D_{real} was set to 5 mm, and P_{total} was set to 9.6 W for both lasers [13]. For the copper distribution, D_{sim} was set to 2 mm. Since the iron particle distribution had a higher average and a higher standard deviation, its D_{sim} was set to 4 mm. The number of rays employed in the simulation, N_{rays}, was set to 5000 for the copper powder and 100 for the iron powder (see Section 4.1 for proof of convergence). The values are summarized in Table 3.2.

Table 3.2: Laser Decomposition Parameters

Powder	P_{total} (W)	N_{rays}	D_{sim} (mm)	D_{real} (mm)	P_{ray} (W)
Copper	9.6	5000	2	5	3.072×10^{-4}
Iron	9.6	100	4	5	6.144×10^{-2}

3.3 Ray Tracing

Once N_{rays} is known and P_{ray} has been calculated, the process of tracing the rays as they pass through the particle packing can be conducted. Figure 3.5 shows a flow diagram of this process.

It starts with the creation of the first ray. When a ray is created, it has three attributes: power (P), initial point ($\vec{p_i}$), and direction ($\vec{v}$). This allows it to be described in parametric form, as shown in Equation 3.5, where d is the scalar progression variable and $p(d)$ is the locus of points that compose the ray. To simplify calculations, $\vec{v}$ is always stored in the normalized form.

$$\vec{p}(d) = \vec{p_i} + \vec{v}d \tag{3.5}$$

After the ray is created, a check is performed to determine whether any particles lie in its path. This is achieved by first sorting the particles in ascending order by their distance from the ray's initial point. The distance along the ray between the ray's initial point and the first particle is then calculated using Equation 3.6, where $\vec{c}$ refers to the particle's center and r refers to the particle's radius. Often, this function produces two values because it describes both the point where the ray enters the particle and the point where the ray exits the particle. Since we are only interested in the former, the smaller of the two values is always used.

$$d_{particle} = -(\vec{v} \cdot (\vec{p_i} - \vec{c})) \pm \sqrt{(\vec{v} \cdot (\vec{p_i} - \vec{c}))^2 - (||\vec{p_i} - \vec{c}||^2 - r^2)} \tag{3.6}$$

The point at which the ray strikes the particle is then found by substituting $d_{particle}$ into Equation 3.5. This point is considered the terminus point, $\vec{p_t}$, of the ray[1], and it is used to generate the refracted ray using the principles described in chapter 3.

If $d_{particle}$ is smaller than zero or complex, then the ray did not intersect that particle. In this case, the Equation 3.6 is applied to the next particle in the sorted list until a real, positive value is obtained or the list is exhausted. If none of the particles produced a real, positive $d_{particle}$ value, then the ray passes through the entire packing without touching any of the particles.

Since the packing does not contain the entire spot area of the laser, periodic boundary conditions have been enforced to simulate the surrounding particles which are not explicitly present. To achieve this, a bounding cylinder has been placed around the packing. If the ray intersects the vertical walls of the cylinder, it continues with same direction from the opposite side of the cylinder. If we use the vector convention shown in Equation 3.7 and Equation 3.8 for p_i and v, respectively, then Equation 3.9 gives the distance along the ray from the ray's initial point to the wall of a bounding cylinder with radius r_c and height h_{cyl}. An additional variable, ϕ, has been introduced to simplify the expression in Equation 3.9. The definition of ϕ is given in Equation 3.10. As with the particle intersections, Equation 3.9 often produces two values (one positive and the other negative) because it follows the ray in both the positive and negative direction. Since we are only interested in the former, the positive value is always used.

$$\vec{p_i} = \langle p_{i_x}, p_{i_y}, p_{i_z} \rangle \tag{3.7}$$

$$\vec{v} = \langle v_x, v_y, v_z \rangle \tag{3.8}$$

$$d_{wall} = \frac{-\phi \pm \sqrt{\phi^2 - 4(v_x^2 + v_y^2)(p_{i_x}^2 + p_{i_y}^2 - r_c^2)}}{2(v_x^2 + v_y^2)} \tag{3.9}$$

[1] Although this technically describes a line segment, the term ray will continue to be used for clarity.

$$\phi = 2[\langle p_{i_x}, p_{i_y} \rangle \cdot \langle v_x, v_y \rangle] \tag{3.10}$$

However, the bounding cylinder also has a floor and ceiling. If we assume the floor is positioned in the $z = 0$ plane and the ceiling is positioned in the $z = h_{cyl}$ plane, then Equation 3.11 and Equation 3.12 give the distance along the ray from the ray's initial point to the cylinder floor and ceiling, respectively.

$$d_{floor} = -p_{i_z}/v_z \tag{3.11}$$

$$d_{ceil} = \frac{h_{cyl} - p_{i_z}}{v_z} \tag{3.12}$$

In all cases, the point of contact is obtained by substituting the calculated distance back into Equation 3.5. This becomes the ray's terminus point, and the trace for that particular ray is considered complete. If the ray contacts the floor or ceiling first, then the process starts over with another ray from the original set. However, if the ray contacts the wall first, then the periodic boundary is enforced by creating a new ray on the opposite side of the cylinder with same direction as the ray that was just completed. If the center of the cylinder floor has been placed at the origin, then the new initial point is given by Equation 3.13.

$$\vec{p}_{i_{periodic}} = \langle -p_{i_x}, -p_{i_y}, p_{i_z} \rangle \tag{3.13}$$

Finally, the power of the reflected ray is checked after each reflection. If the new ray is carrying less than 1% of the incident ray's power, then the ray in question is prevented from reflecting any further. This increases computational efficiency and removes the possibility of a ray bouncing back and forth infinitely.

Figure 3.4 shows a simplified visualization of a ray trace through a copper powder packing. The colors of the rays indicate how much power they are carrying, and the color of the particles indicates how much power they are absorbing.

3.4 Chapter Summary

In this chapter, the methods employed to generate particle packings, discretize the beam into rays, and trace the rays through the powder were described. The experimental parameters that were used to define the powder and laser were given as well. The next chapter presents the results produced by the methods described in this chapter for cases that have been tested experimentally and establishes convergence for those cases. It also shows trends developed by analyzing a range of refractive indices.

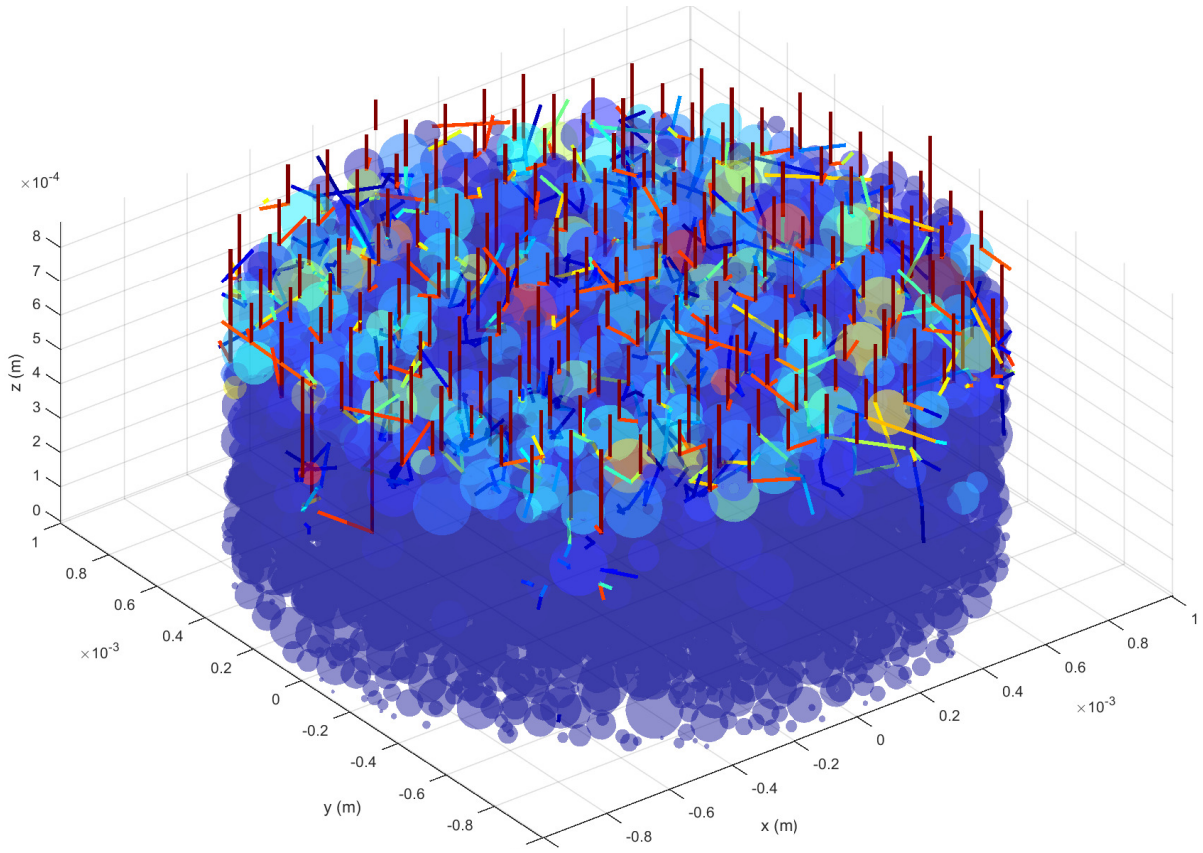

Figure 3.4: Simplified Visualization of a Ray Trace through Copper Powder

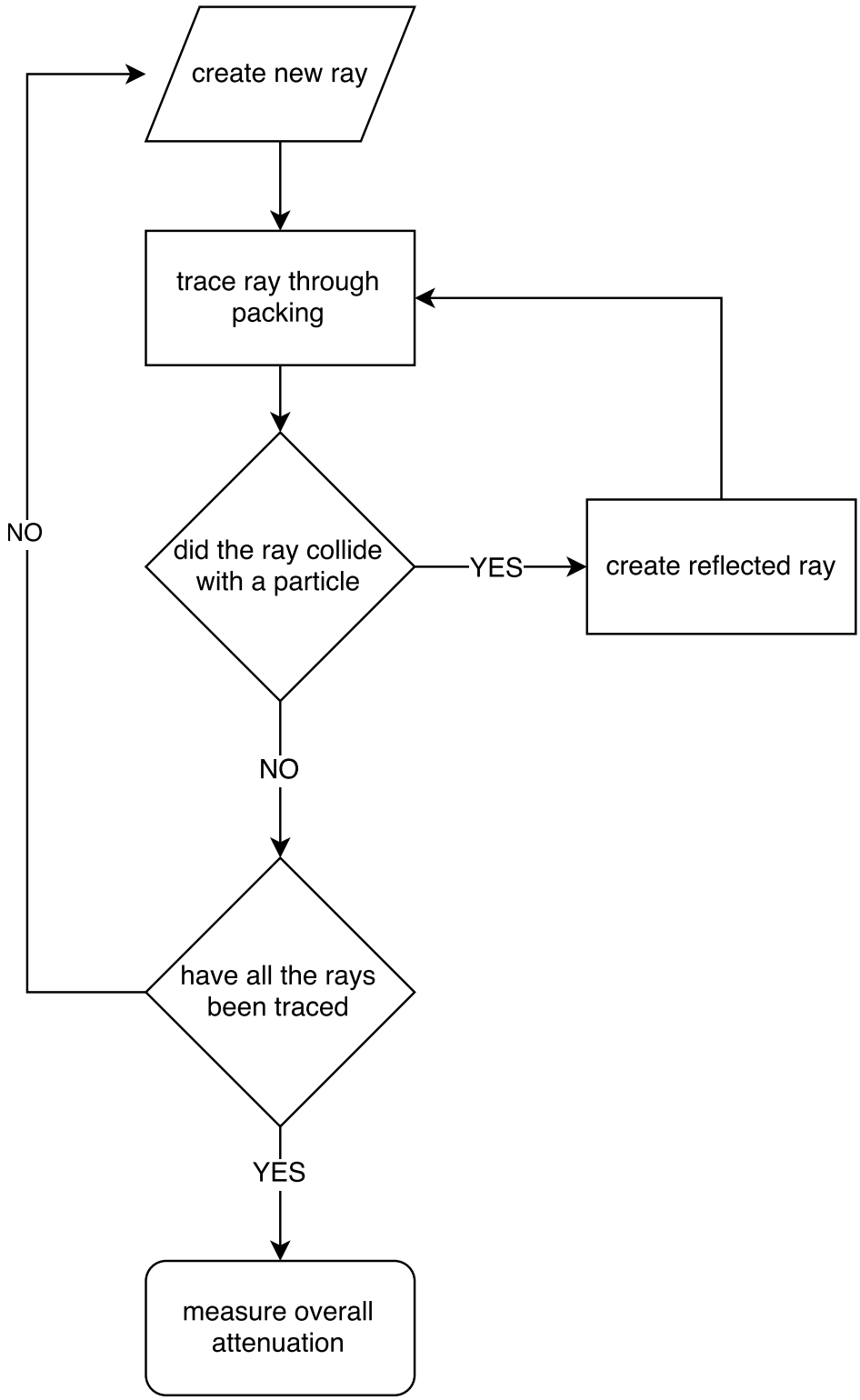

Figure 3.5: Flow Diagram for Ray Tracing Procedure

Chapter 4

Results

This chapter presents the results obtained by applying the methods described in Chapter 3 to cases for which experimental data has been collected. These results are also used to establish convergence for the ray tracing method. Finally, trends are determined by simulating a range of refractive indices.

4.1 Convergence

As mentioned in chapter 2, the fundamental assumption in this work is that reducing a continuous laser beam to a finite number of discrete rays produces accurate results. If the assumption is correct, then increasing the number of rays past some finite number, N_c, does not significantly affect the results. To observe whether this is true, Figure 4.1 and Figure 4.2 plot the calculated attenuation coefficient against the number of rays used in the simulation. Dashed lines mark $\pm 5\%$ error bars with reference to the first data point, marked in solid black, for which the remaining points remain within the error bounds. The number of rays associated with that point is taken to be N_c (see Table 3.2 for a summary of the values).

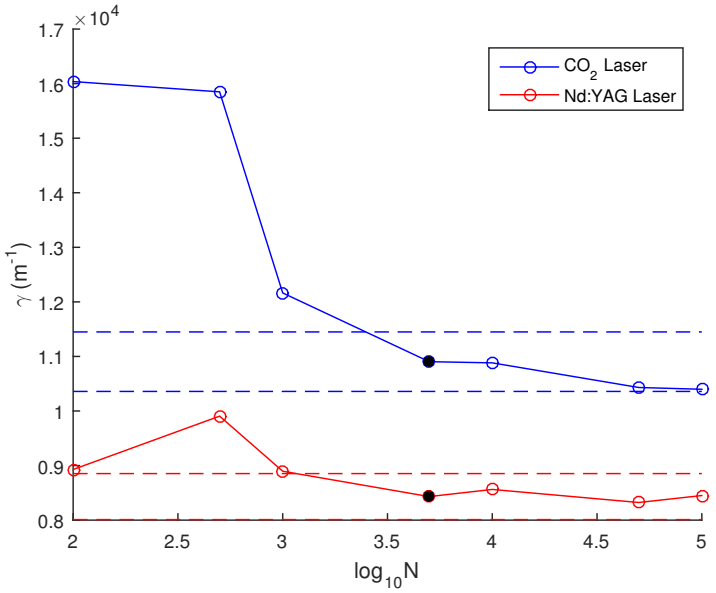

Figure 4.1: Attenuation Coefficient vs. Number of Rays for Copper Powder

4.2 Power Penetration

The main purpose of this investigation is to determine how power was attenuated as the laser passed through the powder. To visualize this, Figure 4.3 plots the penetrated power against the depth for each of the scenarios in question. It is apparent from the figure that the copper powder under a CO_2 laser experienced the least power penetration, while the iron powder under the CO_2 laser experienced the most.

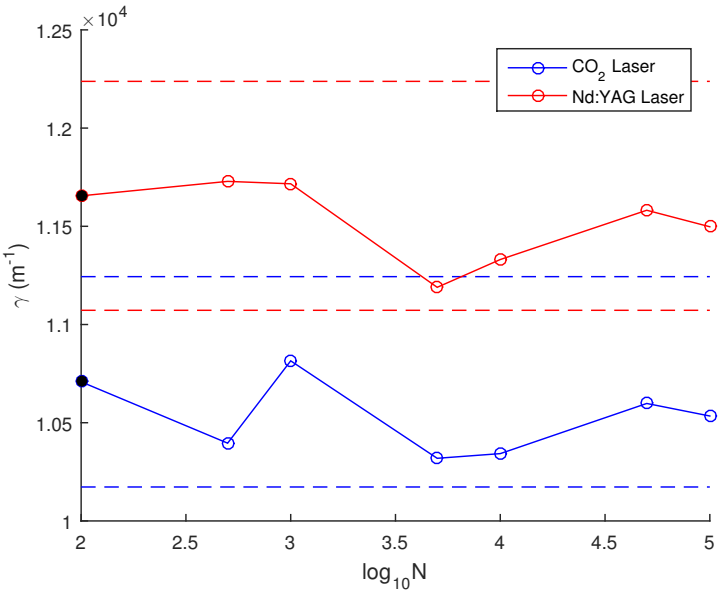

Figure 4.2: Attenuation Coefficient vs. Number of Rays for Iron Powder

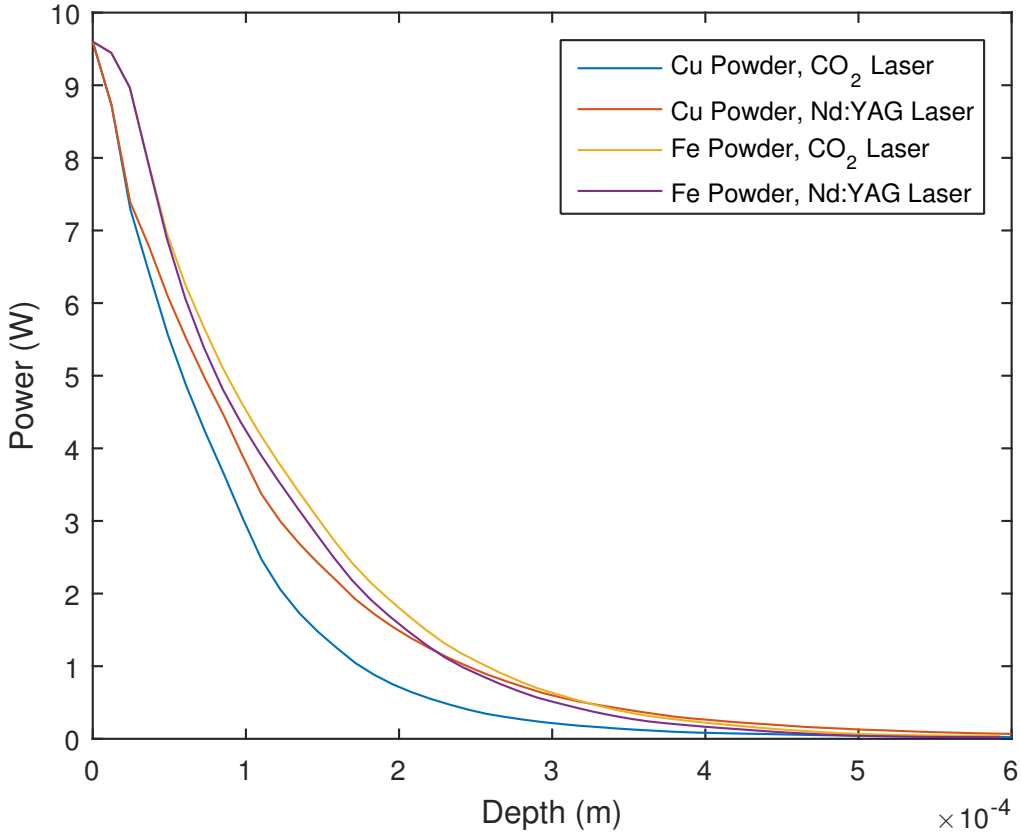

Figure 4.3: Power vs. Depth

4.3 Curve Fit Coefficients

As explained in chapter 2, the attenuation coefficients are obtained by fitting exponential curves to the power vs. depth data. To capture the values that best represent reality, the curves should be fit to the entire domain of the data sets. However, the experimental values against which the simulated results are being compared, shown in Table 1.1[1], were obtained by fitting curves in smaller domains, the limits of which are given in Table 1.2. Therefore, the results of both strategies are presented in Table 4.1. Figures 4.4 to 4.7 show the fits that were calculated using the experimental ranges. The error between the attenuation coefficients computed from the simulated data and those derived from the experimental data is given in Table 4.2. A detailed analysis of the error values is provided in Section 5.1.

Table 4.1: Values for Curve Fits of Simulation Data

Powder	Laser	Computational (full)			Computational (clipped)		
		β	γ (m^{-1})	R^2	β	γ (m^{-1})	R^2
Cu	CO_2	0.7124	1.09E+04	0.9001	6.97E-01	1.13E+04	0.9868
	Nd:YAG	0.8696	8.39E+03	0.9835	0.7922	8.31E+03	0.9990
Fe	CO_2	1.2723	1.00E+04	0.9722	1.52E+00	1.05E+04	0.9998
	Nd:YAG	1.3517	1.11E+04	0.9509	1.83E+00	1.18E+04	0.9999

Table 4.2: Attenuation Coefficient Error Values

Powder	Laser	Computational (full)	Computational (clipped)
Cu	CO2	-16.35%	-13.02%
	Nd:YAG	-25.72%	-26.44%
Fe	CO2	-41.99%	-39.38%
	Nd:YAG	-23.22%	-17.90%

4.4 Index Analysis

One of the advantages of using a computational method to determine power attenuation is that a large number of scenarios can be tested much more efficiently than experimentation would allow. Figure 4.8 plots the attenuation coefficient against a whole range of refractive indices for the two different powder packings that were developed. The curves shown in the figure have a clear asymptote at $n_t = 1$. This is to be expected, since n_i was assumed to be unity as well, and the reflected power goes to zero when $n_i = n_t$ (see Equation 2.3 and Equation 2.4). Notice also that once the refractive index exceeds 2, then the relationship becomes very linear, which is shown by the dashed lines.

[1] Values for β were not reported for the experimental curve fits.

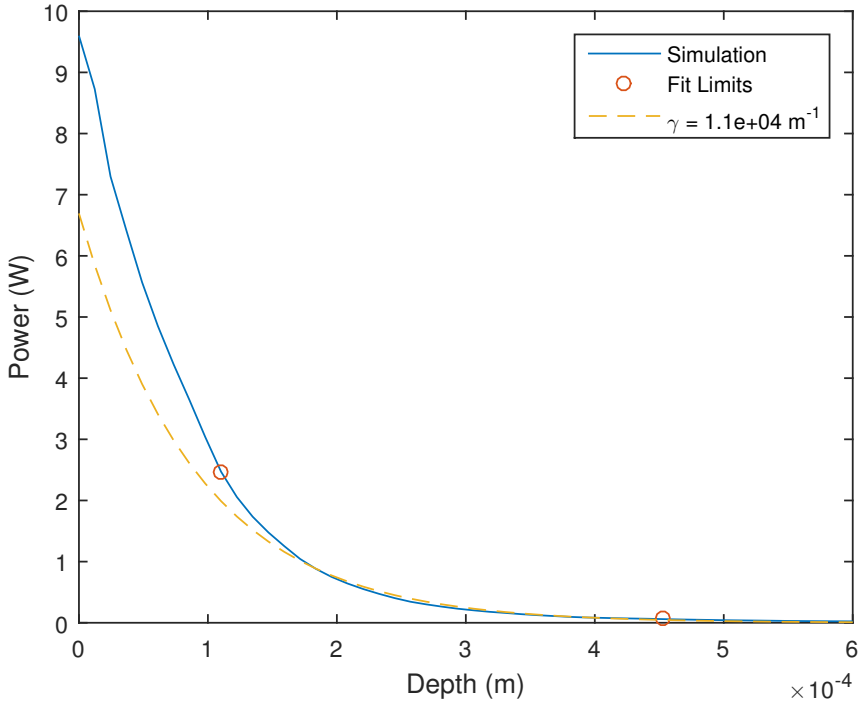

Figure 4.4: Attenuation Coefficient vs. Depth for Copper Powder Under CO_2 Laser

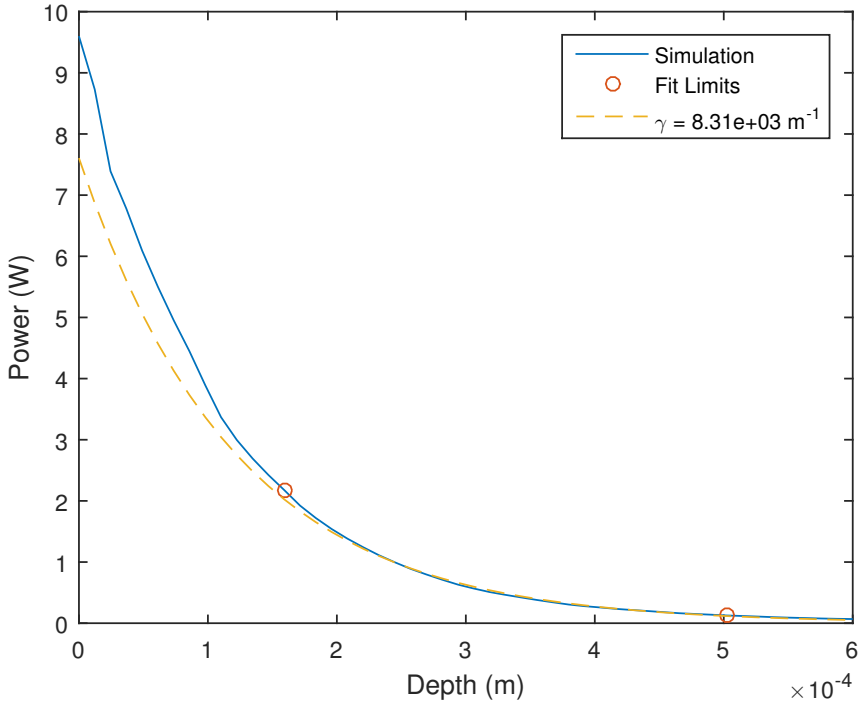

Figure 4.5: Attenuation Coefficient vs. Depth for Copper Powder Under Nd:YAG Laser

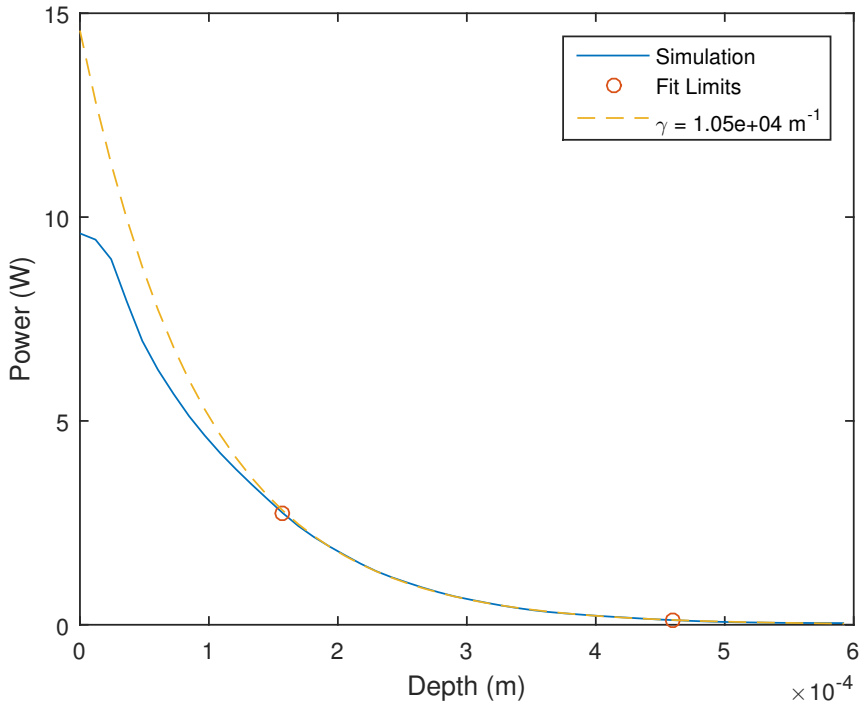

Figure 4.6: Attenuation Coefficient vs. Depth for Iron Powder Under CO_2 Laser

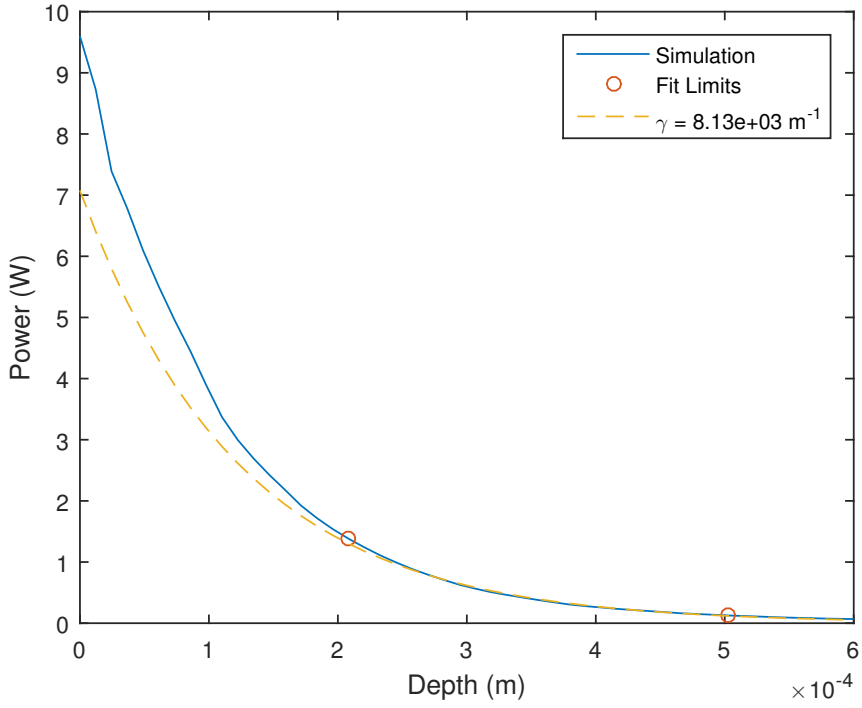

Figure 4.7: Attenuation Coefficient vs. Depth for Iron Powder Under Nd:YAG Laser

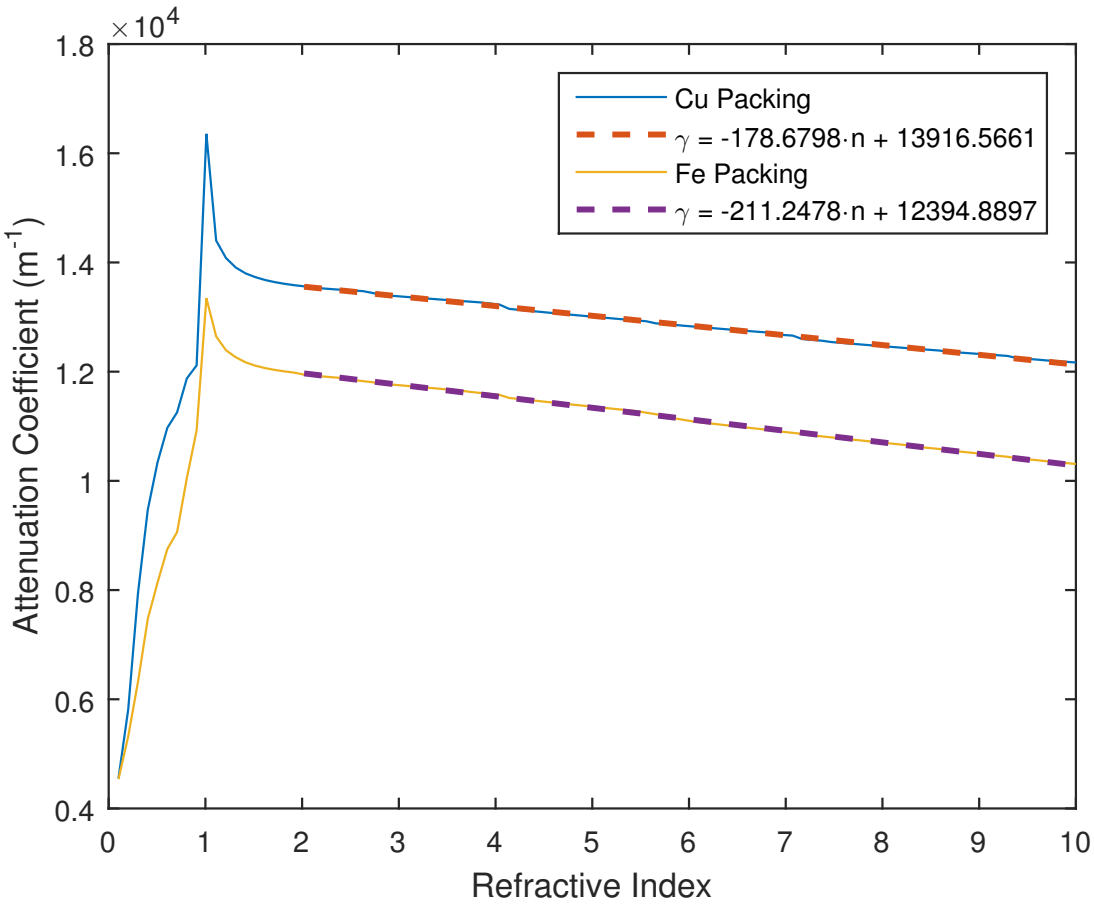

Figure 4.8: Attenuation Coefficient vs. Refractive Index

4.5 Chapter Summary

This chapter served to both established convergence for the ray tracing method and compare computational results to experimental values. Additionally, trends for the relationship between the attenuation coefficient and refractive index were developed for the different powders. The next chapter presents a detailed analysis of the error reported in this chapter and the implications of this work. It also describes possible areas for future work.

Chapter 5

Discussion, Implications, and Future Work

This chapter serves three purposes. First, it provides an analysis of the error values given in Chapter 4. Second, it describes the implications of the work that has been presented, and third, it explores possible areas for future work.

5.1 Error Analysis

The purpose of this work was to determine whether a simple ray tracing algorithm could be used to accurately describe the attenuation of a laser beam as it passes through a powder layer during metal additive manufacturing. As Table 4.2 shows, the error between the calculated results was not insignificant. Overall, the average error was -24.2%. The fact that all of the calculated errors were negative suggests that the simulation is consistently underestimating the attenuation.

A possible reason for this is the formation of oxide layers. Most copper and iron oxides have lower indices of refraction than the pure metals [20] [21]. Figure 2.2 shows that the fraction of power that is absorbed decreases with refractive index for indices that are greater than unity. This means that more power would be absorbed by each layer of particles if the refractive index was lowered by the presence of oxides. The simulation also does not account for surface roughness. If peaks and valleys occurred on the surface of the particles such that reflected rays impacted the same particle from which they were reflected, then the rate of absorption would increase.

However, there is also error in the experimental results that must be considered. Table 1.1 shows that some of the R^2 values for the fits that were applied to the experimental data are far from optimal. For the case of the iron powder under a CO_2 laser, the experimental R^2 value is -3.844, which suggests no correlation. Therefore, it is not surprising that this case also yielded the largest error between the experimental and simulated values.

5.2 Implications

As the error analysis demonstrated, the current form of the ray-tracing algorithm is not sufficient to calculate laser attenuation with a high degree of accuracy. However, the error is small enough that the trends should still be valid, and several important conclusions can be draw from an analysis of these trends.

First, the form of the power vs. depth data conforms very closely to exponential model presented in chapter 2 (see Equation 2.11). Table 4.1 shows that the R^2 values for this relationship are all greater than 0.90, and in the case of the clipped data, none of the R^2 values fall below 0.98. Since the exponential model is very similar to Lambert's Law [22], this suggests that porous powder packings like the ones analyzed might behave like solid mediums with modified properties.

Second, there appears to be very little variation introduced from only analyzing the data ranges described by Table 1.2. The average difference between the attenuation coefficients obtained from fitting the full data and clipped data was 2.34%. This also highlights the sensitivity of the error analysis, because the average 2.34% difference between values generates an average 13.08% difference between the error results of full and clipped data.

Finally, there appears to be a linear relationship between the attenuation coefficient and the refractive index for indices greater than 2, as shown in Figure 4.8. Since most materials of interest satisfy this condition, this relationship could be used to drastically reduce the computing resources

required to predict attenuation coefficients. That cost could be reduced even further if a relationship was developed between the packing properties and the relationships coefficients.

5.3 Future Work

The results of this work suggest several possible areas of focus for future work. As mentioned in Section 5.1, oxides and surface roughness are possible sources of error; so, adjusting the algorithm for these phenomena could be of interest. Both of these pose a certain amount of difficulty. The oxide layers are not usually thick enough to entirely absorb refracted rays; so, additional capabilities would be required to analyze the attenuation through the oxide layer and the interaction at the oxide-metal interface. Surface roughness introduces a level of randomness into the simulation; so, a Monte Carlo component would be required. Both of the challenges are manageable, but their implementation will significantly increase required computing resources.

Additionally, Section 4.4 mentioned that an advantage to a computational approach is the ability to analyze a large number of possible cases. However, the only parameter that was varied for this study was the real component of the refractive index for the powder. Future work could extend the analysis to the complex plane. The density of the packing could also be varied. Again, both of these tasks would be computationally intensive, but they might help develop a more complete picture on how the refractive index and density affects the attenuation coefficient.

Bibliography

[1] S. H. Huang, P. Liu, A. Mokasdar, and L. Hou. Additive Manufacturing and its Societal Impact: a Literature Review. *The International Journal of Advanced Manufacturing Technology*, 67(5-8):1191–1203, 2013.

[2] ASTM Standard. F2792. 2012. Standard Terminology for Additive Manufacturing Technologies. *ASTM F2792-10e1*, 2012.

[3] B. E. Carroll, T. A. Palmer, and A. M. Beese. Anisotropic tensile behavior of ti–6al–4v components fabricated with directed energy deposition additive manufacturing. *Acta Materialia*, 87:309–320, 2015.

[4] Wohlers Associates, Inc. Wohlers Associates Publishes 20th Anniversary Edition of Its 3D Printing and Additive Manufacturing Industry Report. Press Release, April 2015. https://www.wohlersassociates.com/press69.html.

[5] S. Dunham. Metal Additive Manufacturing Trends. http://www.smartechpublishing.com/images/uploads/general/Dunham_RAPID_2015_Metal_Additive_Manufacturing_Trends.pdf. Accessed: 2016-03-20.

[6] P. Michaleris. Modeling Metal Deposition in Heat Transfer Analyses of Additive Manufacturing Processes. *Finite Elements in Analysis and Design*, 86:51–60, 2014.

[7] N. Shen and K. Chou. Thermal Modeling of Electron Beam Additive Manufacturing Process: Powder Sintering Effects. In *ASME 2012 International Manufacturing Science and Engineering Conference collocated with the 40th North American Manufacturing Research Conference and in participation with the International Conference on Tribology Materials and Processing*, pages 287–295. American Society of Mechanical Engineers, 2012.

[8] S. Khairallah and A. Anderson. Mesoscopic Simulation Model of Selective Laser Melting of Stainless Steel Powder. *Journal of Materials Processing Technology*, 214(11):2627–2636, 2014.

[9] F. J. Gürtler, M. Karg, K. H. Leitz, and M. Schmidt. Simulation of Laser Beam Melting of Steel Powders Using the Three-Dimensional Volume of Fluid Method. *Physics Procedia*, 41:881–886, 2013.

[10] J. Zhou, Y. Zhang, and J. K. Chen. Numerical Simulation of Laser Irradiation to a Randomly Packed Bimodal Powder Bed. *International Journal of Heat and Mass Transfer*, 52(13):3137–3146, 2009.

[11] D. Moser, S. Pannala, and J. Murthy. Computation of Effective Radiative Properties of Powders for Selective Laser Sintering Simulations. *JOM*, 67(5):1194–1202, 2015.

[12] T. I. Zohdi. Rapid Simulation of Laser Processing of Discrete Particulate Materials. *Archives of Computational Methods in Engineering*, 20(4):309–325, 2013.

[13] R. W. McVey, R. M. Melnychuk, J. A. Todd, and R. P. Martukanitz. Absorption of Laser Irradiation in a Porous Powder Layer. *Journal of Laser Applications*, 19(4):214–224, 2007.

[14] J. W. Shirley. An Early Experimental Determination of Snell's law. *American Journal of Physics*, 19(9):507–508, 1951.

[15] M. B. Kraichman. *Handbook of Electromagnetic Propagation in Conducting Media*. Headquarters Naval Material Command: for sale by the Supt. of Docs., US Govt. Print. Off., 1970.

[16] M. S. Dresselhaus. *Solid State Physics Part II Optical Properties of Solids*. Citeseer, 1999.

[17] M. Polyanskiy. Refractive Index Database. http://refractiveindex.info/. Accessed: 2016-03-01.

[18] A. Lakhtalda. Would Brewster Recognize Today's Brewster Angle? *Optics News*, page 15, 1989.

[19] V. Šmilauer et al. Yade documentation 2nd ed. *The Yade Project*, 2015.

[20] K. Mörl, U. Röpke, B. Knappe, J. Lehmann, R. Perthel, and H. Schröder. Optical Properties of Sputtered Fe_2O_3 films. *Thin Solid Films*, 60(1):49–53, 1979.

[21] G. Papadimitropoulos, N. Vourdas, V. Vamvakas, and D. Davazoglou. Optical and Structural Properties of Copper Oxide Thin Films Grown by Oxidation of Metal Layers. *Thin Solid Films*, 515(4):2428–2432, 2006.

[22] D. F. Swinehart. The Beer-Lambert Law. *Journal of Chemical Education*, 39(7):333, 1962.

ACADEMIC VITAE OF
CHRISTOPHER D. KOZUCH

Education

The Pennsylvania State University — **Graduated May 2016**
University Park, PA
- Bachelor of Science in Mechanical Engineering
- Minor in Mathematics

Work Experience

The Boeing Company — **May 2015 – Aug. 2015**
Structural Testing Intern — St. Louis, MO
- Designed hydraulic load assemblies for large scale structural testing
- Performed finite element analysis to ensure the integrity of designs
- Supervised material testing of composites and analyzed results
- Wrote VBA script for analyzing material properties associated with mode I crack growth in composites

Sandia National Laboratories — **May 2014 – Oct. 2014**
Computational Simulation Intern — Albuquerque, NM
- Created a C++ path planning program for the additive manufacture of advanced shock absorbers
- Designed critical components using topology optimization codes
- Implemented new error handling system for a large software package

Kennametal, Inc. — **May 2013 – Aug. 2013**
Lathe Technology Intern — Latrobe, PA
- Employed programmable optical microscopy to perform quality analysis measurements on lathe insert geometries
- Developed MATLAB algorithms and codes to process collected data and run surface roughness simulations
- Modified a variety of product drawings using Siemens NX

The Pennsylvania State University — **Feb. 2013 – May 2015**
Laboratory Assistant — University Park, PA
- Assisted students with SolidWorks modeling and design projects
- Aided professor with lectures and demonstrations
- Provided grade assessment and proctored exams

Research

Penn State Applied Research Laboratory — **Oct. 2014 – May 2015**
Distinguished Undergraduate Researcher — University Park, PA
Current Objectives:
- Produce MATLAB algorithm for determining the laser energy absorbed by powders during the additive manufacture of metals
- Experimentally validate aforementioned algorithm

Penn State Computational Biomechanics Group — **Sep. 2013 – May 2015**
Undergraduate Research Assistant — University Park, PA
- Wrote medical image processing program for high resolution modeling of trabecular bone microstructure
- Performed finite element analysis on the human calcaneus
- Developed algorithm for inserting artificial porosity into bone models

Publications

R. A. Fielding, R. H. Kraft, X. G. Tan, A. J. Przekwas and C. D. Kozuch, "High Rate Impact To The Human Calcaneus: A Micromechanical Analysis," in *2014 ASME IMECE*, Montreal, 2014. — **November 2014** Montreal, Québec

Awards

- William & Wyllis Leonhard Engineering Scholar
- Schreyer Honors Scholar
- Dean's List Every Semester

Positions Held

American Society of Mechanical Engineers – Penn State Chapter — **Sept. 2012 - Present**
University Park, PA

Secretary (Aug. 2013 – May 2014)

- Prepared officer meeting agendas and recorded meeting minutes
- Recorded events, correspondences, and meeting attendances

Webmaster (Aug. 2015 – Present)

- Created new website using open source templates

American Solar Energy Society – Penn State Chapter — **Sept. 2012 - Present**
University Park, PA

Vice President (Aug. 2014 – May 2015)

- Organized community tour of local solar tour installations
- Coordinated guest speakers for general body meetings

Skills

C++	SolidWorks	Linux	CUBIT
MATLAB	Siemens NX	Windows	ABAQUS